The Planetary Science Journal, 1:73 (14pp), 2020 December https://doi.org/10.3847/PSJ/abb942

Convex Shape and Rotation Model of Lucy Target (11351) Leucus from Lightcurves and Occultations

Stefano Mottola[1], Stephan Hellmich[1], Marc W. Buie[2], Amanda M. Zangari[2,4], Simone Marchi[2], Michael E. Brown[3], and Harold F. Levison[2]
[1] Institute of Planetary Research, DLR Rutherfordstr. 2, D-12489 Berlin, Germany; stefano.mottola@dlr.de
[2] Southwest Research Institute 1050 Walnut Street, Boulder, CO 80302, USA
[3] California Institute of Technology 1200 E. California Boulevard, Pasadena, CA 91125, USA
Received 2020 July 6; revised 2020 September 1; accepted 2020 September 15; published 2020 December 8

Abstract

We report new photometric lightcurve observations of the Lucy Mission target (11351) Leucus acquired during the 2017, 2018, and 2019 apparitions. We use these data in combination with stellar occultations captured during five epochs to determine the sidereal rotation period, the spin axis orientation, a convex shape model, the absolute scale of the object, its geometric albedo, and a model of the photometric properties of the target. We find that Leucus is a prograde rotator with a spin axis located within a sky-projected radius of 3° (1σ) from J2000 Ecliptic coordinates ($\lambda = 208°$, $\beta = +77°$) or J2000 Equatorial Coordinates (R.A. = 248°, decl. = +58°). The sidereal period is refined to $P_{\rm sid} = 445.683 \pm 0.007$ h. The convex shape model is irregular, with maximum dimensions of 60.8, 39.1, and 27.8 km. The convex model accounts for global features of the occultation silhouettes, although minor deviations suggest that local and global concavities are present. We determine a geometric albedo of $p_V = 0.043 \pm 0.002$. The derived phase curve supports a D-type classification for Leucus.

Unified Astronomy Thesaurus concepts: Light curves (918); Stellar occultation (2135); Jupiter trojans (874); CCD photometry (208)

Supporting material: machine-readable table

1. Introduction

Jupiter Trojans are a class of small objects trapped in the Jupiter L4 and L5 Lagrangian points. Their origin is still disputed, with the most likely scenarios falling into the categories (1) coeval trapping of local planetesimals in the 1:1 mean motion resonance with accreting Jupiter as a consequence of drag or collisions (Yoder 1979; Shoemaker et al. 1989) or (2) post-Jupiter-formation capture of scattered trans-Neptunian planetesimals following an episode of orbital chaos (Morbidelli et al. 2005) during the orbital migration of the giant planets or as a consequence of the Jumping Jupiter scenario as defined in Nesvorný et al. (2013). In either case, Trojans are thought to be primitive objects that experienced little thermal evolution and contain a considerable amount of volatiles, which makes them close relatives to cometary nuclei.

With a launch planned for 2021 October, Lucy is the thirteenth NASA mission of the Discovery Program and will be the first one to explore the Jupiter Trojan System. Its trajectory is designed to fly by five Trojans—one of which, (617) Patroclus is an equal-size binary system—distributed over the two Lagrangian clouds. The encounter with Leucus is currently planned for 2028 June 18. A coordinated effort has been initiated to support the mission with a systematic program of ground-based observations of the mission targets aiming at characterizing their dynamical, physical, rotational, and photometric properties. The goal is to inform the mission design in order to maximize the scientific return of the encounters and to complement the space-based measurements with data that are most efficiently acquired from the ground.

This paper presents new lightcurve photometry of the Lucy target Leucus, which is used, together with the results of stellar occultation campaigns presented in a companion paper (Buie et al. 2020), to determine its convex shape, spin axis orientation, albedo, size, sphere-integrated phase curve, and *V*–*R* color index.

2. Leucus

(11351) Leucus belongs to the Jupiter L4 Trojan swarm. Radiometric measurements by the IRAS satellite reported a size and a geometric albedo of 42.2 ± 4.0 km and 0.063 ± 0.014, respectively (Tedesco et al. 2004). Grav et al. (2012) reported a size and an albedo of 34.155 ± 0.646 km and 0.079 ± 0.013, respectively, based on Wide-field Infrared Survey Explorer (WISE) radiometry. Levison & Lucy Science Team (2016) tentatively classified Leucus as belonging to the D taxonomic type based on its visible spectral slope (Roig et al. 2008). No collisional family membership has been proposed as of today. French et al. (2013) first realized from lightcurve data that Leucus is a very slow rotator, although they identified an incorrect period of 515 h. Buie et al. (2018), using photometric observations acquired during the 2016 apparition, combined with observations by French (2013), determined a firm rotation period of 445.732 ± 0.021 h. They also estimated a geometric albedo of 0.047 based on the WISE diameter and on an average color index for D-type asteroids.

3. Observations and Data Reduction

The new Leucus photometric observations reported in this paper were performed during its 2017, 2018, and 2019 apparitions by using 1.0 m telescopes from the Las Cumbres Observatory

[4] Amanda Zangari is currently an MIT Lincoln Laboratory employee. No laboratory funding or resources were used to produce the results/findings reported in this publication.

Table 1
Observational Circumstances

Date (UT)	λ (° J2000)	β (° J2000)	α (°)	r (au)	Δ (au)	λ (PAB) (° J2000)	β (° J2000)	Band	Observatory	Observers
2017 May 1.1	287.4	+5.7	9.683	5.507 1	5.032 0	282.5	+5.5	R_C	493	SH, SMo
2017 May 2.1	287.4	+5.8	9.616	5.506 7	5.017 5	282.6	+5.5	R_C	493	SH, SMo
2017 May 20.1	287.0	+6.3	7.887	5.500 5	4.774 5	283.0	+5.9	R_C	493	SH, SMo
2017 May 28.1	286.5	+6.6	6.841	5.497 7	4.685 2	283.1	+6.1	R_C	493	SMo, SH
2017 May 30.1	286.3	+6.6	6.550	5.497 0	4.664 6	283.1	+6.1	R_C	493	SMo, SH
2017 May 31.0	286.3	+6.6	6.408	5.496 6	4.655 1	283.1	+6.1	R_C	493	SMo, SH
2017 Jul 16.4	281.0	+7.6	2.738	5.479 8	4.491 4	282.2	+6.9	r'	Q64	MWB, AZ
2017 Jul 17.0	280.9	+7.6	2.833	5.479 5	4.493 2	282.1	+6.9	r'	W86	MWB, AZ
2017 Jul 17.3	280.9	+7.6	2.882	5.479 4	4.494 2	282.1	+6.9	r'	W85	MWB, AZ
2017 Jul 17.6	280.8	+7.6	2.933	5.479 3	4.495 2	282.1	+6.9	r'	Q63	MWB, AZ
2017 Jul 17.9	280.8	+7.6	2.980	5.479 2	4.496 2	282.1	+6.9	r'	K93	MWB, AZ
2017 Jul 18.2	280.8	+7.6	3.031	5.479 1	4.497 3	282.1	+6.9	r'	W86	MWB, AZ
2018 Jun 11.1	318.3	+11.1	9.382	5.339 4	4.745 1	313.5	+10.5	R_C	493	SH, SMo
2018 Jul 9.1	316.6	+12.1	5.829	5.326 3	4.437 9	313.8	+11.1	V	493	SH, SMo
2018 Jul 15.0	316.0	+12.2	4.895	5.323 6	4.394 7	313.8	+11.2	V	493	SH, SMo
2018 Sep 4.9	309.8	+12.5	6.171	5.299 0	4.436 2	312.8	+11.5	V	493	SH, SMo
2018 Aug 6.9	313.2	+12.7	2.406	5.312 7	4.318 6	313.3	+11.5	R_C	493	SH, SMo
2018 Aug 8.0	313.1	+12.7	2.432	5.312 3	4.318 7	313.3	+11.5	R_C	493	SH, SMo
2018 Aug 9.0	312.9	+12.7	2.475	5.311 8	4.319 2	313.3	+11.5	R_C	493	SH, SMo
2019 Nov 9.1	342.2	+12.6	10.103	5.101 6	4.597 6	347.3	+12.0	VR	G80	MWB
2019 Nov 10.1	342.2	+12.6	10.181	5.101 2	4.611 2	347.4	+12.0	VR	G80	MWB
2019 Nov 11.1	342.2	+12.5	10.257	5.100 8	4.624 9	347.4	+12.0	VR	G80	MWB
2019 Nov 12.1	342.2	+12.5	10.329	5.100 4	4.638 7	347.5	+11.9	VR	G80	MWB
2019 Nov 24.1	342.6	+12.0	10.962	5.095 5	4.812 3	348.2	+11.7	VR	G80	MWB

Note. This table is an excerpt. The observational circumstances for all of the observation nights are reported in the online material. λ and β are the topocentric ecliptic longitude and latitude of the target, respectively. α is the solar phase angle, r is the heliocentric distance, and Δ is the topocentric range of Leucus. λ and β (PAB) are the topocentric ecliptic longitude and latitude of the phase angle bisector, as defined in Harris et al. (1984).

(This table is available in its entirety in machine-readable form.)

Global Telescope (LCOGT) network, the 1.2 m telescope at the Calar Alto Observatory, Spain, and the two 24″ telescopes sited at Sierra Remote Observatories (SRO), Auberry, CA, USA, owned and operated by Southwest Research Institute (SwRI). The observational circumstances are detailed in Table 1. Typical exposure times were of 5 minutes for the Calar Alto observations, with the telescope tracked at half the relative tracking rate of the asteroid, in order to reduce smearing and obtain equal point-spread functions (PSFs) for the target and field stars. The LCOGT observations were also exposed for typically 5 minutes, but were tracked at object rate, since those telescopes do not support halfway tracking.

The SRO systems use an Andor Xyla sCMOS camera with a maximum exposure time of 30 s. All data taken on Leucus used this maximum exposure time. In 30 s, the motion of Leucus is 125 mas at opposition, corresponding to less than half of a pixel smear and even a smaller fraction of the PSF. The very fast readout and low read noise of the sCMOS camera nearly eliminate the penalties of taking such short exposures. During processing, we can stack as many images as desired to reach an signal-to-noise (S/N) goal. Two stacks are built from the data, one registered on the stars and the other registered on the apparent motion of Leucus. We can use image subtraction to remove the stars in the Leucus stack but this was not necessary for the 2018 and 2019 data from SRO. For these data we chose to stack 10 images at a time and used synthetic aperture integration to retrieve the photometry of Leucus, thus providing an effective integration over 5 minutes. The star-stacked images were used with the same aperture to determine the instrumental magnitudes of the stars.

This raw photometry was further binned in time by a factor of 3 to increase the per-point S/N while also allowing the estimation of a good uncertainty for the photometry.

For the observations from Calar Alto, most fields were measured with *Himmelspolizey*, a reduction pipeline developed by SH. The latter implements a semiautomatic astrometric/photometric workflow that uses SExtractor (Bertin & Arnouts 1996) for photometric extraction, an optimistic pattern matching algorithm (Tabur 2007) for astrometric reduction, and a moving object detection algorithm for asteroid identification as described in Kubica et al. (2007). In the case of crowded fields, synthetic aperture photometry was measured interactively with AstPhot (Mottola et al. 1995).

The observations proved to be challenging mainly for two reasons. First, during the 2017 apparition the target was still close to the Galactic center, which implied that involvement of the source with field stars was extremely frequent. This issue was dealt with by applying star subtraction. For the observations taken from the LCOGT Network the subtraction was performed in the image domain by applying the method described in Buie et al. (2018). For the observations from Calar Alto, the subtraction was performed in the intensity domain by separately measuring the flux of the involved stars at many epochs distant from the time of the respective appulses. Although star subtraction mitigates the contamination problem, it is not a perfect solution. While the flux of the polluting star is

removed, the photon noise associated with the subtracted flux still contributes to the degradation of the total S/N, sometimes being the dominant contribution. In the latter cases the affected frames were excluded altogether from the data set. Furthermore, imperfect background source removal, due, e.g., to changing seeing conditions during the observations, results in a non-Gauss distribution of the measurements error which can cause outliers in the data that can be difficult to discern.

The second challenging aspect was the very long rotation period of the target, which caused a useful night of observations to produce data points only at a single rotational aspect. As a consequence, a large number of nights over extended periods of time were needed to ensure complete rotational coverage. Furthermore, the resulting data set virtually consisted only of sparse photometry in the sense that subsequent nights' observations did not overlap in rotation phase, preventing compilation of a composite lightcurve from relative photometry. Composite lightcurves were therefore generally constructed based on absolute photometry, with the disadvantage of the additional uncertainty component due to the errors of the calibration zero-points. Fortunately, modern, all-sky photometric catalogs with very good coverage, limiting magnitude, and accuracy have become available in recent years, so the problem of the accuracy of the zero-point is not as severe as it has been in the past. With the fields of view of our detectors, a large number of suitable photometric catalog stars was always simultaneously present in the same frame as the target, allowing us to identify variable stars and outliers. For the observations from LCOGT, carried out with the SDSS r' filter, we used the APASS photometric catalog (Henden et al. 2012). For the Calar Alto observations, carried out in the Johnson V and Cousins R_C filters, we used the Gaia DR2 catalog (Gaia Collaboration et al. 2018) with the transformations from the G photometric band from Evans et al. (2018). The observations from the SRO were performed with a VR broadband filter. Gaia DR2 field stars were used to express the asteroid in the Gaia G bandpass without further transformation or color correction.

Typically, relative photometric accuracy of the individual points (binned points for the SRO) ranged from 0.01 to 0.03 mag rms. The absolute photometric accuracy of the zero-points was typically of the order of 0.02 mag rms. For all observations, the magnitudes were reduced to 1 au from the Sun and the observer. The times were converted to the Barycentric Dynamical Time (TDB) frame, in order to provide a uniform time reference. Further, the times were corrected for the one-leg, target-observer light-travel time.

For the purpose of compact representation—but not for model computation—the photometric time series were compiled into composites for each individual apparition. This was achieved by performing a Fourier series fit of the fourth order to determine the respective best-fit synodic periods by using the procedure described in Harris et al. (1989). Normally, we would fit simultaneously the Fourier coefficients and a phase function to absolute photometry data in order to compensate for brightness changes due to the phase curve. The implicit assumption is that the shape of the lightcurve—in particular its amplitude—remains constant over a few consecutive rotational cycles. While this is a reasonable assumption for most asteroids, in the case of Leucus, given its very slow rotation, the amplitude of the lightcurve can change over consecutive rotational cycles due to the change in viewing and observing geometry. Fitting the phase function simultaneously with the rotation period would tend to compensate for the change in the lightcurve amplitude by skewing the phase function, which could result in varying phase curve slopes for different apparitions. For this reason we performed the composites with a nominal linear phase coefficient $\beta = 0.0395$ mag/° for all of the observations reported in this paper (see Section 4.5).

The composite lightcurves for the 2017, 2018, and 2019 apparitions are reported in Figure 1. It can be seen that the respective synodic periods differ among each other by as much as 0.7 h, which corresponds to about 0.15%. This is expected for two reasons. First, due to the slow rotation, the useful baseline for the determination of the periods for each apparition covers just a handful of rotational cycles, which limits the accuracy of the determination. Second—and to a lesser extent—the apparent instantaneous rotation rate depends on the rate of change of the topocentric ecliptic longitude of the object, which can make the synodic period change slightly during the course of an apparition and from one apparition to the next. In the next sections we will derive a very accurate sidereal period and phase function by using a dynamical and shape model that makes use of all of the available observations over a baseline of about 6 years.

4. Modeling

4.1. Data

The photometric lightcurves presented in the previous section and in Buie et al. (2018), and the results from the stellar occultation campaigns reported in Buie et al. (2020) constitute the bulk of observational data used for our modeling work. In addition, we made use of dense lightcurve photometry by French et al. (2013; retrieved through the ALCDEF service (http://alcdef.org/)) and sparse photometry from the following sources:

1. The Gaia DR2 database (Gaia Collaboration et al. 2018) retrieved through the VizieR server (https://vizier.u-strasbg.fr/),
2. The ZTF project (Bellm et al. 2019) retrieved through the IRSA server (https://irsa.ipac.caltech.edu/applications/ztf/) and from the nightly transient archive at https://ztf.uw.edu,
3. The PAN-STARRS-1 DR2 database (Flewelling et al. 2016) retrieved through a query to the MAST archive (https://catalogs.mast.stsci.edu/), and
4. The ATLAS project (Tonry et al. 2018) retrieved through the AstDys database (https://newton.spacedys.com/astdys/).

For all but the ATLAS observations, photometric uncertainties were retrieved along with the magnitude data. In the case of the ATLAS observations, we estimated nominal photometric uncertainties by compiling the data into composites for the individual oppositions and computing their residuals. Since the survey observations were acquired in a variety of different photometric systems, for which transformations to the Johnson system are not accurately established, they were treated as relative photometry. Similarly to the dense data set, the times were light-time corrected, and the magnitudes reduced to 1 au. Although these additional data sets provide varying degrees of accuracy, they proved to be very useful to extend the coverage

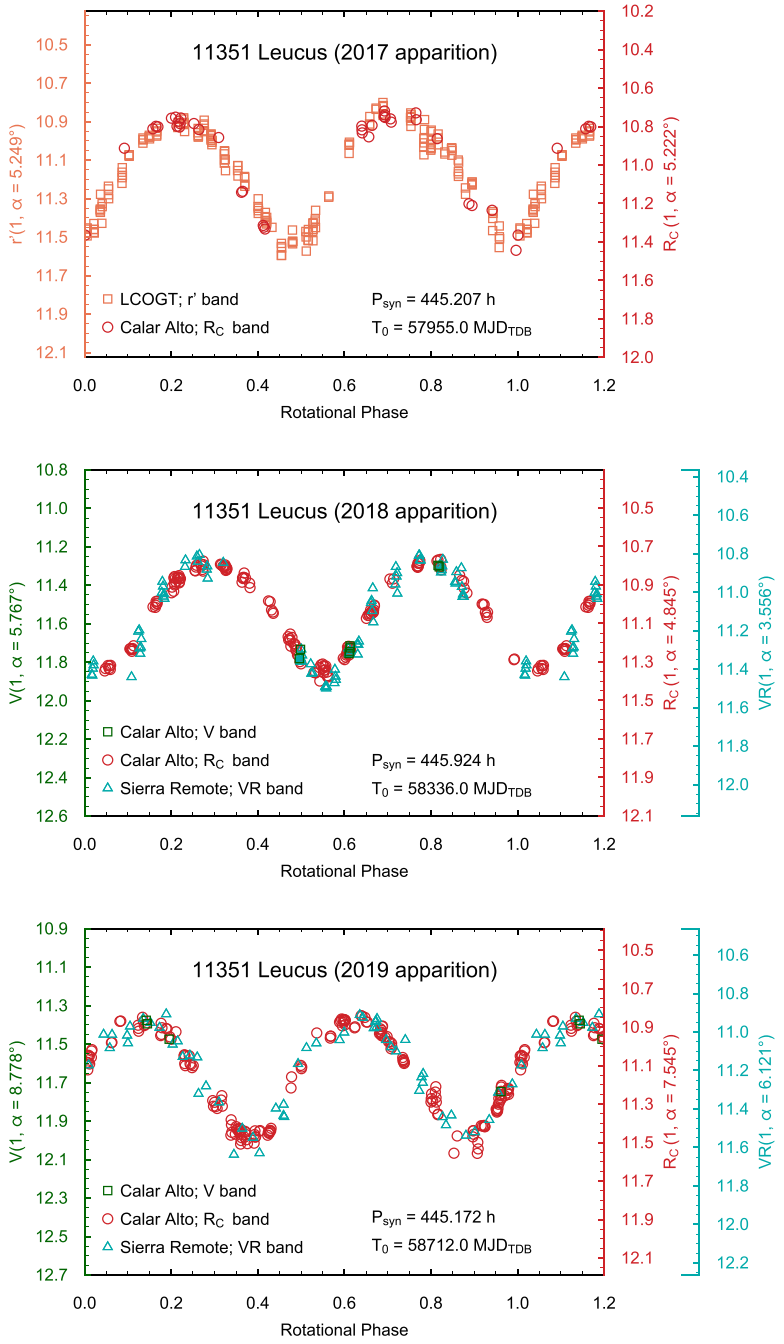

Figure 1. Composite lightcurves for the 2017, 2018, and 2019 apparitions. The data points are folded with the synodic periods listed in the respective graphs, with zero phase corresponding to the respective T_0 epochs. T_0 are one-leg, light-travel time corrected Modified Julian Dates (MJD) expressed in the TDB uniform time frame. The listed synodic periods are the exact numbers used for folding the composites, and as such, are reported without uncertainty. Data points beyond rotation phase 1.0 are repeated for clarity. The magnitudes are reduced to 1 au from both the observer and the Sun and to the respective reference phase angles by using a nominal linear phase coefficient of $\beta = 0.0395$ mag/°.

and baseline of the observations, which combined, cover a period of about 6 years.

4.2. Convex Inversion

In this paper we apply the convex shape inversion approach described in Kaasalainen et al. (2002) and references therein to the photometric time series to simultaneously solve for the sidereal period, the spin-axis orientation, the photometric function, and a convex, polyhedral approximation of the shape. The occultation data are used as a constraint to resolve the spin-axis ambiguity, to determine the scale of the object—and hence its albedo—and to refine the orientation of the spin axis. Although it is likely that Leucus does contain some degree of global-scale concavity, we did not feel that the available data—both because of coverage and photometric accuracy, in the case of lightcurve data, and because of limited unique observation geometries in the case of occultation data—would allow addressing the intrinsic nonuniqueness of the nonconvex problem. On the other hand, the convex inversion scheme offers the advantage of a provably convergent method that results in a unique solution in the case of a convex shape (Kaasalainen & Lamberg 2006) and gracefully degrades in the

case of moderate concavities. Nonconvex modeling of Leucus will be the subject of future work as soon as more data—especially at further occultation geometries—become available. Although a working implementation of the convex inversion algorithm (*convexinv*) is publicly available (Durech et al. 2010) we decided to develop our own implementation based on the original publications (Kaasalainen & Torppa 2001; Kaasalainen et al. 2001). This approach has allowed us to overcome some limitations of the code (described later) to expand its functionality and to correct a minor bug in the computation of the χ^2 metric that is present in the current *convexinv* version and that has been promptly communicated to its author. Although we did not make use of any code from *convexinv*, we did use that software to validate the results of our own code on a few test cases.

The surface brightness of the object is described through its photometric function, which, for the purpose of this work, is assumed to be separable into a *disk function* and a *surface phase function* (see, e.g., Schröder et al. 2013). Following Kaasalainen et al. (2001), we adopt Lommel-Seelinger-Lambert (LSL) scattering as a disk function and a three-parameter exponential-linear combination as a surface phase function, as described in the Appendix. The LSL disk function is the linear combination of the Lommel-Seeliger and Lambert scattering functions through a partition parameter c and is equivalent to the Lunar-Lambert disk function (Li et al. 2015 and references therein) when the latter is used with a partition function independent of the phase angle. We fixed c to a constant value of $c = 0.1$, appropriate for dark asteroids (Kaasalainen et al. 2005). For this work we did not attempt to use more complex photometric models—as, e.g., the Hapke function (Hapke 2012 and references therein), because due to the small phase-angle range in which Trojans can be observed from Earth, no meaningful retrieval of the model parameters is achievable.

The brightness of the object depends on the product of its size and its albedo. From unresolved photometric measurements alone, it is not possible to retrieve independently those two quantities. Independent measurements such as thermal radiometry, stellar occultations, or direct imaging, however, offer the possibility to disentangle the two quantities. In the absence of more detailed information, we assume that the photometric properties of the target—in particular its albedo—are uniform over its surface. This is quite a reasonable assumption, because, although albedo variations on asteroids do occur, the observed lightcurve variations tend to be dominated by the changing cross-section of a nonspherical shape.

The convex inversion scheme models the brightness of the target in the space of its Extended Gaussian Image (EGI; Kaasalainen & Torppa 2001), as opposed to the 3D object space. The EGI represents the discrete equivalent of the inverse of the Gaussian Surface Density and is used to represent the area of the facets oriented toward a particular direction. For the Leucus model we parameterize the EGI with a spherical harmonic expansion of rank and order eight, which results in a total of 81 shape parameters, one of which represents its scale. An exponential-function representation of the EGI is used to guarantee positive surface areas. We integrate the EGI over the unit sphere by sampling the spherical harmonics expansion at discrete points by following a Lebedev quadrature (Lebedev & Laikov 1999), which offers greater efficiency compared to a quadrature based, e.g., on a uniform or random sampling (Kaasalainen et al. 2012). In the case of Leucus, we applied a Lebedev rule of order 302, which results in an EGI with the same number of facets.

Contrary to Kaasalainen & Torppa (2001)—and to the *convexinv* implementation—we minimize a weighted metric for solving the least-squares problem in order to properly account for the varying degree of accuracy of the different data sets. In the case of absolute observations, the optimization is performed by minimizing the reduced $\chi^2_{\rm red}$ metric defined as

$$\chi^2_{\rm red} = \frac{1}{N}\sum_i \frac{(L_i^{\rm obs} - L_i^{\rm mod})^2}{\sigma_i^2}, \quad (1)$$

where $L_i^{\rm obs}$ and $L_i^{\rm mod}$ are the observed and model intensities, respectively, σ_i is the intensity uncertainty, and N is the number of degrees of freedom for errors. The index i runs over all of the n photometric data points.

In the case of relative observations, we minimize the deviations of the intensities relative to the average of the respective lightcurve:

$$\chi^2_{\rm rel} = \frac{1}{N}\sum_{k,j}\left(\frac{\bar{L}_j^{\rm obs}}{\sigma_{k,j}}\right)^2\left(\frac{L_{k,j}^{\rm obs}}{\bar{L}_j^{\rm obs}} - \frac{L_{k,j}^{\rm mod}}{\bar{L}_j^{\rm mod}}\right)^2, \quad (2)$$

where the index k runs over the data points of the lightcurve j and $\bar{L}_j^{\rm obs}$ and $\bar{L}_j^{\rm mod}$ are the average intensities of the observed and modeled lightcurve j, respectively. The term $\sigma_{k,j}$ represents the uncertainty of the kth data point of lightcurve j. If absolute observations were performed during the same apparition in two photometric bands, then a color index term is introduced to tie the two photometric systems. The color term is also optimized in the procedure. If, on the other hand, one photometric band is never used together with another photometric system at least during one apparition, then these series of observations are treated as relative photometry in order to avoid a possible parameter coupling between the color index and the spin-axis orientation. The nonlinear optimization is performed with the Levenberg–Marquardt algorithm (Press et al. 1992).

A unique transformation from the EGI to a polyhedron in 3D space is guaranteed by a Minkowski theorem (Minkowski 1897). For this transformation we use the iterative scheme proposed by Lamberg (1993). The body reference system is defined such that the Z-axis coincides with the spin axis. The plane that contains the body center of mass and that is perpendicular to the Z-axis defines the XY plane in the body system. The direction of the X-axis is chosen such that it coincides with the projection of the principal axis of smallest inertia onto the XY plane. The body X-axis also defines the location of the prime meridian and thus the zero longitude.

4.3. Rotation Model

The rotation period strongly modulates the spectrum of the χ^2 of the fit with periodic local minima at a minimum spacing $\Delta P \approx P^2/(2T)$ (Kaasalainen et al. 2001), where P is the rotation period and T is the total baseline of the lightcurve coverage. It is therefore important that the optimization be started in the vicinity of the correct period in order to avoid the optimizer becoming trapped in the local minimum of an alias period. For this reason, the search of the correct sidereal period is the first step in the convex inversion scheme. The search is

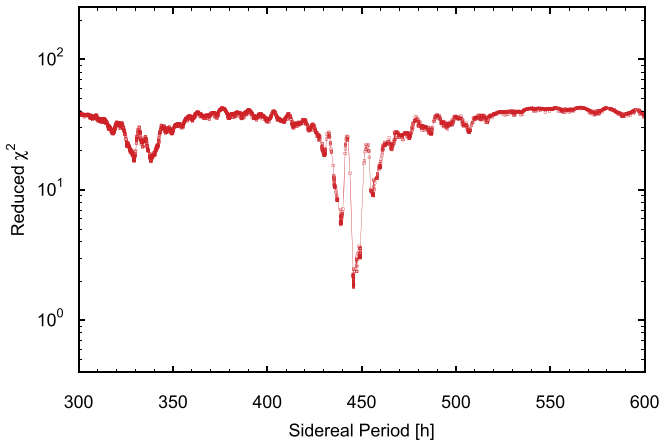

Figure 2. Result of the sidereal period scan. Each data point corresponds to a local-minimum solution obtained by using trial periods in the range between 300 and 600 h as iteration start values for the sidereal period. The global minimum around 445.7 h corresponds to the best-fit solution.

performed by running the inversion procedure using all trial periods in a relevant range as starting conditions with a step sufficiently smaller than the minima separation. For each trial period we use 12 different starting pole directions. Figure 2 shows the results of the period scan for Leucus.

In order to identify the coarse direction of the spin axis we run the optimization procedure using the best-fit sidereal period derived in the previous paragraph as a starting value and by fixing the spin-axis orientation to each of about 20,000 trial directions equally spaced on the celestial sphere. The shape of the object, the sidereal period, and the photometric parameters (but not the pole coordinates) are simultaneously optimized for each trial pole. The resulting χ^2 values for each solution are mapped on the celestial sphere via a polar azimuthal equidistant projection and are shown in Figure 3. As expected, two equally significant loci for the best solution are identified. This is the consequence of the *ambiguity theorem* (Kaasalainen & Lamberg 2006) that states that if disk-integrated photometric observations are always carried out in the same photometric plane—as is the case for low-inclination objects observed from Earth—then two indistinguishable solutions exist that satisfy the observations and that are separated by about 180° in ecliptic longitude. The shapes corresponding to the two solutions are approximately mirrored shapes of one another around the body *XY*-plane. The graph also shows that both solutions are prograde and, as already inferred by Buie et al. (2018), the obliquity of the spin axis is low.

4.4. Fit to the Occultation Data

By providing disk-resolved information, occultation data can resolve the pole ambiguity, fix the absolute scale of the shape model, and, together with the determined H_V-value, measure its geometric albedo.

In principle, occultation data can also be used to derive nonconvex shape models provided sufficient, densely sampled silhouettes are available at multiple rotation phases. Much work has been recently done concerning the optimal fusion of data coming from disk-integrated photometry and disk-resolved techniques as stellar occultations, adaptive-optics direct imaging, and interferometry (e.g., Kaasalainen & Viikinkoski 2012; Viikinkoski et al. 2015). In the case of Leucus, however, both the limited lightcurve coverage and the sparse silhouette sampling would not allow a reliable nonconvex model to be derived. For this reason we decided to adopt an approach similar to Durech et al. (2011) and favor the advantages of the uniqueness and stability of a convex solution.

For each of the two best-candidate solutions from the previous section we project the vertices of the shape model onto the plane of sky at the time of each occultation event and then compute the 2D convex hull of the projected points. Applying this procedure to the two complementary solutions visible in Figure 3 allowed us to unambiguously identify the correct solution as the one centered at an ecliptic longitude of around 210°. However, it also became apparent that the best solution had a slight systematic deviation in the orientation of the projection with respect to the occultation data that could be explained by a slight offset (≈5°) in the direction of the spin-axis orientation of the model. Such a small mismatch was not unexpected, as the loci of the solutions in Figure 3 are quite broad and shallow, and a small shift in the spin axis direction of the model would produce fits to the lightcurves with similar χ^2. On the other hand, disk-resolved data such as stellar occultations are much more sensitive to a pole misalignment. For this reason we decided to use the occultation data for the refinement of the solution.

As a goodness of fit for the occultation data we define a metric

$$\chi^2_{\rm occ} = \sum_{i,j} \frac{(D_{ij})^2}{N_{\rm op}}, \tag{3}$$

where D_{ij} represents the minimum Euclidean distance between the occultation transition point j (either ingress or egress) of the event i and the model 2D convex hull of the event i. $N_{\rm op}$ is the total number of the observed transition points. This metric is different from the one chosen by Durech et al. (2011), who prefer to use the distance of the occultation points to the occultation limb measured in the direction of the asteroid ground track. Their choice is justified by the fact that the largest contribution to their occultation data is given by timing errors and observer reaction times, which act along track. In our case, on the other hand, we estimate the largest errors to be due to the convex-shape model, which are not expected to have a preferred direction.

$\chi^2_{\rm occ}$ is minimized by optimizing the global scale and the Cartesian coordinates of the centers of the projections for each occultation epoch. The latter is necessary to compensate both for inaccuracies in the position of the occulted stars and for the uncertainties of the target ephemeris at the epochs of the occultations. In practice the minimization is performed by varying the projection centers and the $A_{\rm LSL}$ albedo (see the Appendix)—which constrains the scale—in an adaptive grid search fashion.

One practical problem arises from the fact that the convex-shape optimization is performed in the EGI space, while the occultation profile optimization is done in the space of the projected shape. It is therefore impractical to perform a simultaneous, combined optimization. For this reason we used the $\chi^2_{\rm occ}$ as a mild penalty function for a combined $\chi^2_{\rm tot}$ of the form

$$\chi^2_{\rm tot} = \chi^2_{\rm conv} + \lambda \chi^2_{\rm occ}, \tag{4}$$

where $\chi^2_{\rm conv}$ is the term coming from the convex inversion and λ is a small weight. The value of λ has been determined by

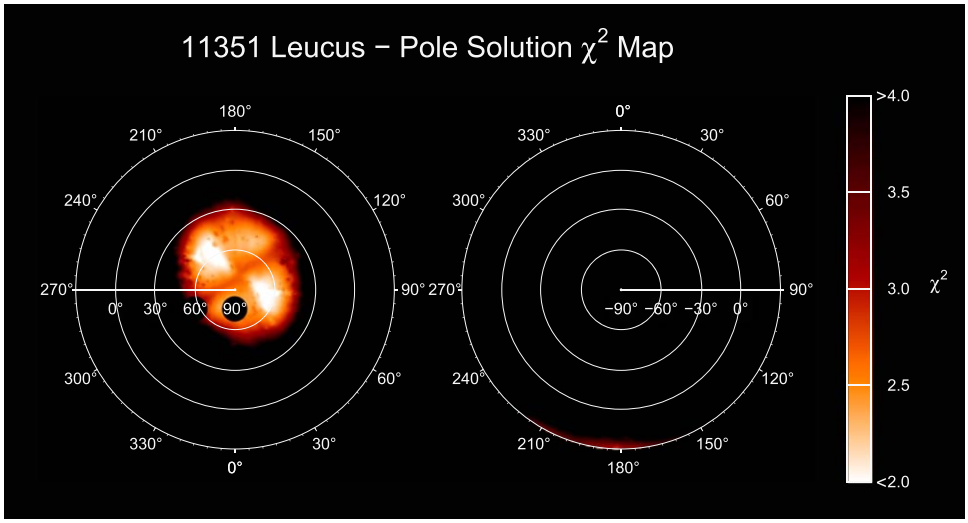

Figure 3. Polar azimuthal equidistant projection of the χ^2 of the pole solutions. The coordinates are expressed in the J2000 ecliptic frame. The left panel is centered on the north ecliptic pole and the right one on the south ecliptic pole. The loci of the two complementary best solutions are clearly visible as white regions.

experimentation by adopting a value of λ that minimized $\chi^2_{\rm occ}$ without significantly increasing $\chi^2_{\rm conv}$. We have then computed the quantity $\chi^2_{\rm tot}$ for one hundred discrete pole directions within a radius of 10° of the best solution (and of the complementary one).

The parameters for the best-fit solution are reported in Table 2. The errors quoted for the different quantities have been determined by computing perturbed solutions and investigating the effects on the χ^2. It must be noted that this method produces an evaluation of the statistical component of the uncertainties only. The largest contribution to the errors is thought to be due to the violations of the assumptions, as the assumption of the functional form of the photometric model and the convexity assumption. Those contributions, however, are virtually impossible to formally quantify. For this reason we refrained from using more sophisticated statistical error models, such as the Markov Chain Monte Carlo (MCMC) method, because they also only address the stochastic component of the uncertainty.

Figure 4 shows the synthetic lightcurves for the corresponding shape model for the epochs covered by the dense observations reported in this paper. The lightcurve intensities are corrected for changing heliocentric and topocentric range and are normalized to unity at the maximum of the respective observation window. Besides the rotational variation, the intensity variation due to the changing phase angle is visible.

Figure 5 shows the resulting best-fit model overplot onto the occultation chords by Buie et al. (2020). The complementary (wrong) solution is also plotted in light gray, showing how occultation data can help identify the correct solution. Please note that, for comparison purposes, we plot the data following Buie's convention of projecting the shape onto the plane of sky (Green 1985), with the η coordinate increasing toward celestial north and the ξ coordinate increasing toward east. This is a different convention than in Durech et al. (2011) who project the shape onto the fundamental plane, with the η coordinate increasing toward west and the ξ coordinate increasing toward north.

We note that the model shape well reproduces the occultation profiles and captures the general shape of the object within the limits of a convex representation. In particular, it reproduces well the flat sides visible during the events LE20181118 and LE20191002 and the polygonal appearance of event LE20181118. It is also important to note that the occultation data are not directly used to derive the convex shape. The shape is influenced by the occultation data only indirectly through the

Table 2
Results

Sidereal Period (h)	445.683 ± 0.007
Pole J2000 Ecl. Longitude (°)	208
Pole J2000 Ecl. Latitude (°)	+77
Pole J2000 R.A. (°)	248
Pole J2000 Decl. (°)	+58
Radius of pole uncertainty (°, 1σ)	3
Ecliptic obliquity of pole (°)	13
Orbital obliquity of pole (°)	10
T_0 (JD_{TDB})	2 456 378.0
Φ_0 (°)	−76.129
W_0 (°)	60.014
$\dot{W}$ (°day^{-1})	19.385 96 ± 0.00030
p_V	0.043 ± 0.002
A_{LSL}	0.061 ± 0.002
A_0	0.23 ± 0.09
D (rad)	0.075 ± 0.015
k (rad^{-1})	−1.07 ± 0.23
c (fixed)	0.1
H_{V-LSL} (sph. int.)	10.979 ± 0.037
H_{V-lin} (sph. int.)	11.034 ± 0.035
β (mag/°)	0.039 5 ± 0.0005
H_{V-HG} (sph. int.)	10.894 ± 0.004
G	0.34 ± 0.02
$H_{V-HG_1G_2}$ (sph. int.)	10.95 ± 0.01
G_1	0.63 ± 0.04
G_2	0.23 ± 0.02
$V - R$	0.464 ± 0.015
$V - r'$	0.313 ± 0.021
L_X(km)	60.8
L_Y(km)	39.2
L_Z(km)	27.8
Surface-equivalent spherical diam. (km)	41.0 ± 0.7
Photometric surface (km^2)	5288 ± 180
Volume (km^3)	$\leqslant 3.0 \times 10^4$

Note. Please refer to the text for the definition of the respective quantities.

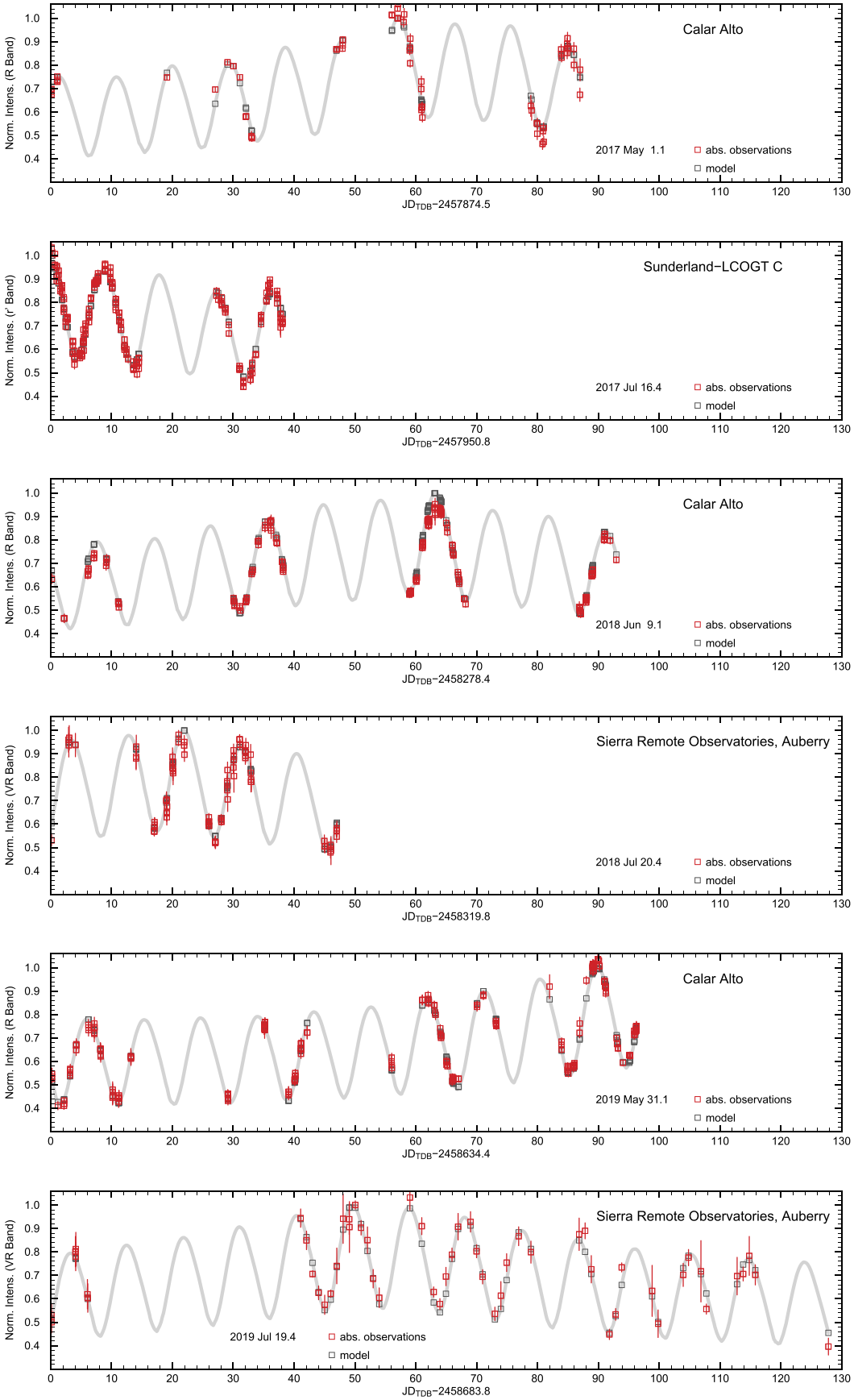

Figure 4. Observed lightcurves shown along with the respective model lightcurves. The data are plotted in intensity and are normalized to unity at the model maximum value for the respective opposition. The dates reported in the labels represent the epoch of the first observation of each sequence.

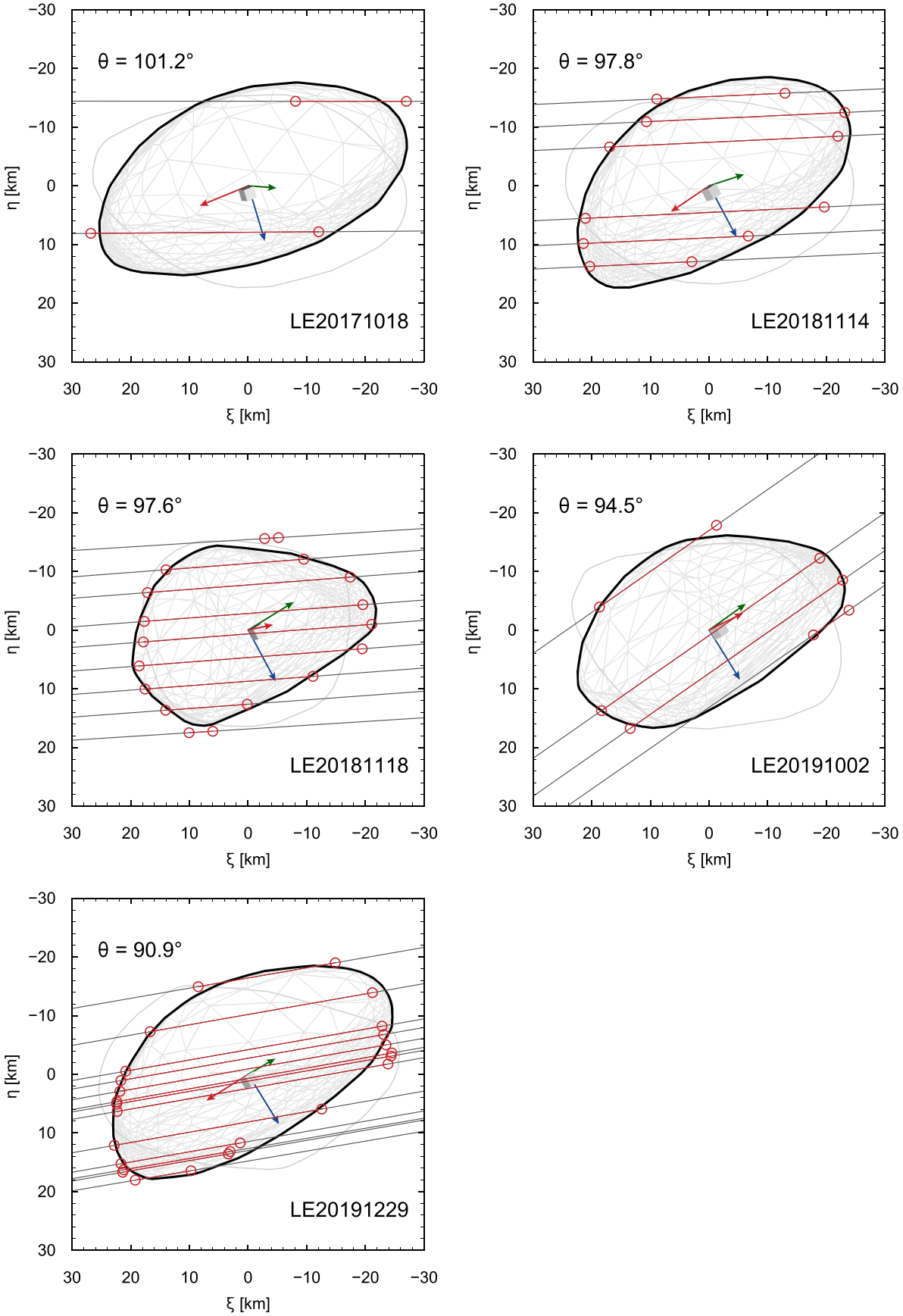

Figure 5. Occulting silhouettes of the best-fit convex model of Leucus (solid black line) along with the rejected complementary model displayed in light gray. The five panels correspond to the epochs of the five occultation events reported in Buie et al. (2020). The red circles correspond to the starts and ends of the respective positive occultation chords. The red, green, and blue arrows represent the *X*, *Y*, and *Z* axes in the body-fixed reference frame, respectively. θ represents the aspect angle, i.e., the angle between the spin axis and the target-observer direction.

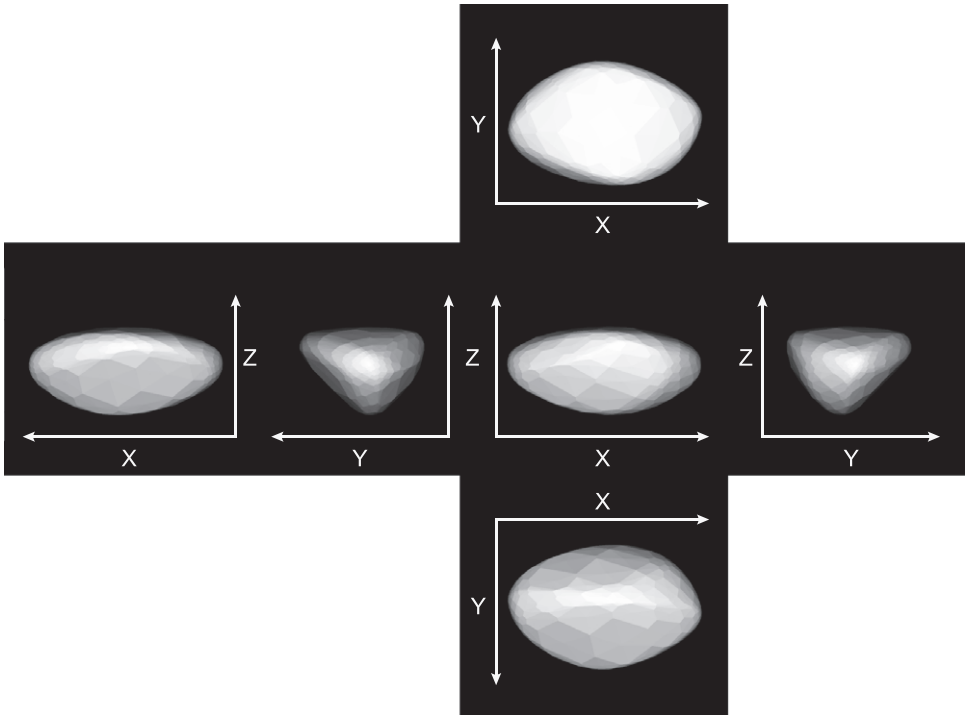

Figure 6. Six orthogonal projections of the best-fit Leucus convex shape arranged similarly to an unfolded die. For contrast reasons, Lambert shading is used for the figure rendering instead of the LSL disk function used in the modeling.

refinement of the spin-axis orientation. In this light, the match of the convex shape model to the occultation data appears even more convincing.

Figure 6 shows six orthogonal views of the best-fit Leucus shape model. As already hinted by the occultation silhouettes, Leucus' shape considerably deviates from an ellipsoid and is characterized by a comparatively flat northern hemisphere. The convexity residual of the shape model resulting from the Minkowski transformation (Kaasalainen & Torppa 2001) is a mere 0.14%, which, taken at face value, would suggest negligible global-scale concavities. However, the small phase-angle range at which observations are available reduces the diagnostic value of this parameter.

As a sanity check, we computed the model's inertia tensor with the method of Dobrovolskis (1996)—assuming a uniform bulk density—and established that the principal inertia axis is misaligned with respect to the body's rotation axis by about 8°. To this end, we have to recall that the derived shape model represents a convex approximation of the shape and ignoring concavities can contribute to shift the direction of the inertia axes. Also the assumption of uniform bulk density, if violated, would contribute to shifting the direction of the principal axis of inertia. The observed misalignment is therefore not necessarily a hint that the object is not in a principal rotation state. Rather, it is an expression of the fact that the convex shape represents a *photometric shape*, which can locally differ from the physical shape.

The maximum extent of a complex shape can be defined in several different ways (see, e.g., Torppa et al. 2008). For our model we define the maximum dimensions as

$$\begin{aligned} L_X &= \max(x_1,...,x_i) - \min(x_1,...,x_i) \\ L_Y &= \max(y_1,...,y_i) - \min(y_1,...,y_i) \\ L_Z &= \max(z_1,...,z_i) - \min(z_1,...,z_i), \end{aligned} \quad (5)$$

where (x_i, y_i, z_i) represent the Cartesian coordinates of the ith vertex of the shape model and the X, Y, and Z body axes are defined as per Section 4.2. This definition produces similar—but not identical—extents as the overall dimensions (OD) definition of Torppa et al. (2008; see their Figure 1). In particular, with our definition, the largest extent is computed in the general direction of the principal axis of the smallest inertia, which represents a natural axis of the body. In the case of the OD definition by Torppa et al. (2008), on the other hand, the maximum dimension is the largest extent that occurs anywhere in the XY plane. As an example, for a hypothetical body with a rectangular equatorial cross-section, with our definition, the maximum extent would be represented by the longest side of the rectangle, while, according to the definition by Torppa, the maximum extent would be represented by the diagonal of the rectangle.

With our definition, the maximum dimensions for Leucus are $L_X = 60.8$ km, $L_Y = 39.2$ km, and $L_Z = 27.8$ km (see Table 2). Those compare with the axes 63.8, 36.6, and 29.6 km of the ellipsoidal approximation by Buie et al. (2020) which were derived under the assumption of a strictly equatorial aspect during the occultation events. In the same table, the orientation of the model is described both by reporting the ecliptic J2000 coordinates of the spin axis and initial angle Φ_0 at the epoch T_0 using the formalism by Kaasalainen et al. (2001) as well as using the IAU convention of reporting the ICRF equatorial coordinates of the spin axis and the W_0 angle at the standard epoch J2000 (Archinal et al. 2018, 2019).

The surface-equivalent spherical diameter of the convex model is $D = 41.0 \pm 0.7$ km whereas its volume is $(30 \pm 2) \times 10^3$ km^3. It should be noted, however, that due to the likely presence of concavities, the quoted value for the volume rather represents an upper bound.

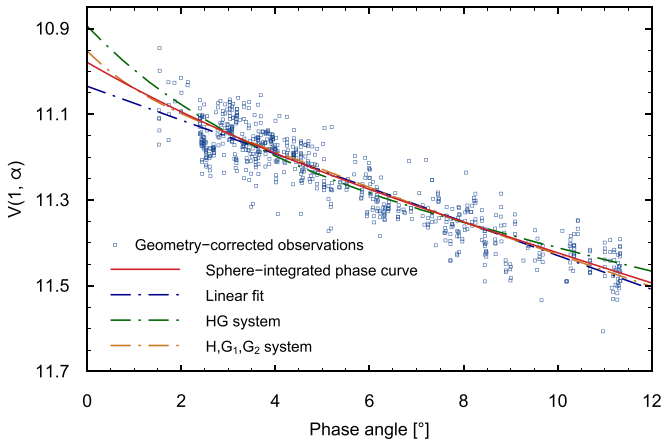

Figure 7. Sphere-integrated phase curve obtained by integrating the best-fit LSL photometric function over a sphere (red solid curve). The blue squares represent the single photometric points for which absolute calibrations and transformations to the Johnson *V* band were available. Those data points have been corrected by multiplying the intensity of the original photometric measurement by the ratio of the intensity of the spherical model to that of the best-fit convex shape model. In this way the effects of changing viewing and observing geometry as well as the rotational variations are removed. The remaining scatter in the data is mostly due to the SNR of the measurements and to the uncertainty in the zero-points of the absolute calibrations. A fit to the data by using the IAU HG system, the HG_1G_2 system, and a linear phase function are also shown for comparison.

4.5. Sphere-integrated Phase Curve

The disk-integrated phase curve of an object condenses the often complex parameter space of a photometric function into a two-dimensional space. As such, the phase curve is a useful phenomenological tool to compare and classify different objects and to infer the presence of physical phenomena, such as, e.g., coherent backscattering. A practical difficulty in deriving phase curves, however, is that during a single apparition—and even more so across multiple apparitions—in addition to the phase angle, other viewing and illumination angles also change (i.e., aspect angle and photometric obliquity), which affects the phase curves. This effect is more pronounced the more the object deviates from a sphere. Having determined through modeling the surface phase function, however, it is possible to compute the phase curve that the object would display if it were a sphere, freeing it from any dependence on the shape and thus being only the expression of the photometric properties of the surface regolith. This is achieved by integrating the photometric function over a sphere in a range of phase angles, as detailed in the Appendix. This representation, which we refer to as the *sphere-integrated phase curve* corresponds to the *reference phase curves* defined by Kaasalainen et al. (2001) in the particular case of a sphere. Figure 7 shows the sphere-integrated phase curve for the LSL photometric function for Leucus (red line) corresponding to the best-fit photometric parameters derived in Section 4.4 and listed in Table 2. For the purpose of comparison, fits are also shown for (1) the best-fit linear phase function ($\beta = 0.0395$ mag/°), (2) the IAU HG system (Bowell et al. 1989), and (3) the more recently adopted IAU HG_1G_2 system (Muinonen et al. 2010). The latter was computed with the online tool described in Penttilä et al. (2016).

As already apparent during the 2016 apparition (Buie et al. 2018), and as observed for several other Trojans (see, e.g., Shevchenko et al. 2012), Leucus has a very subtle—if at all—opposition effect. Within the observed phase angle range, all of the phase curves except for the HG curve—which shows systematic variations both at the small and at the large end of the phase-angle range—provide a good fit to the data. The extrapolation at zero phase produces $H_{V-\mathrm{lin}}$ and $H_{V-HG_1G_2}$ values that differ from the LSL solution (H_{V-LSL}) by about 0.05 mag and 0.03 mag, respectively. These small deviations are partly due to the fact that no calibrated data were available in the *V* band below the phase angle of about 1°.6 to constrain the fit. Buie et al. (2018) did observe Leucus in the r' band at phase angles as low as 0°.125 during the 2016 apparition. However, there appear to be calibration inconsistencies between the 2016 observations and those acquired at the LCOGT in 2017 that are not fully understood. For this reason the 2016 observations were used as a relative data set and do not contribute to our phase curve. It has long been realized (see, e.g., Oszkiewicz et al. 2012; Shevchenko et al. 2016 and references therein) that a correlation exists between an asteroid's taxonomic class and the shape of its phase curve. The above-mentioned tool by Penttilä et al. (2016) also performs an unsupervised taxonomic classification based on the derived HG_1G_2 solution. Interestingly, the software classifies Leucus as a D type, solely based on its phase curve. This further supports the tentative classification by Levison & Lucy Science Team (2016) that was based on spectral information.

It is also important to recall that since Leucus has a considerably larger equatorial cross-section than the polar one, oppositions with a pole-on aspect would result in measured phase curves that are brighter than the sphere-integrated phase curve and conversely, apparitions with an equator-on aspect would appear fainter than the spherical model. Given the low obliquity of Leucus' spin axis, however, all apparitions tend to be at a near-equatorial aspect, as observed from Earth, and therefore Leucus never exposes its largest cross-section to the observer. This effect must be considered, e.g., when computing spherical-equivalent diameters from observations.

4.6. Albedo

The geometric albedo is quite an elusive quantity to measure. First, it is defined for an observation geometry (0° solar phase angle) that is rarely observable from Earth and in which the photometric behavior of different planetary surfaces can wildly vary. Second, it is the result of an indirect measurement that requires the brightness at zero phase and a further measurement as a thermal flux or a geometric cross-section, which adds to the total error budget. Third, the albedo depends in principle on the shape of the object, although this issue is less of a problem for dark objects than for Trojans. The error on the brightness at zero phase directly translates into the same relative error for the geometric albedo (i.e., a 10% error in the brightness would cause a 10% error in the albedo). In our case the geometric albedo is derived through the simultaneous fit of the photometric lightcurves and the occultation data and by applying Equation A3, which results in an accurate geometric albedo determination $p_V = 0.043 \pm 0.002$.

Grav et al. (2012) report for Leucus a much higher geometric albedo of $p_V = 0.079 \pm 0.013$ and a spherical-equivalent diameter $D = 34.155 \pm 0.646$ km derived from WISE observations. Those values are clearly incompatible with the occultation footprints. Part of the reason for their overestimation of the albedo is that they used an inaccurate $H_V = 10.70$, retrieved from the Minor Planet Center database. Very often, those photometric measurements are acquired in

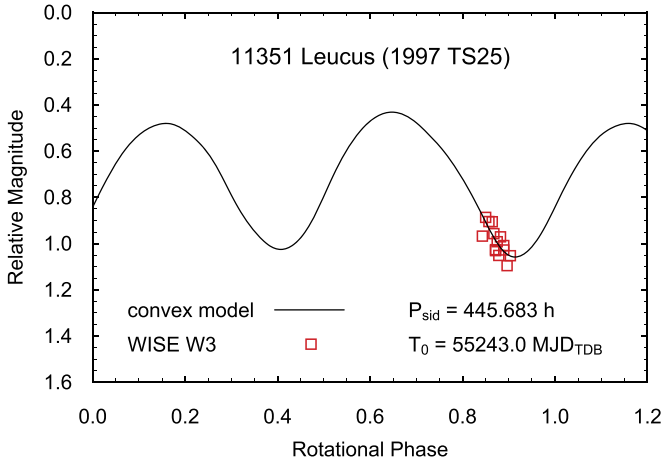

Figure 8. WISE observations (Grav et al. 2012) in the W3 12 μm thermal band are phased with a synthetic lightcurve from our convex model for the same epoch. Data points beyond rotational phase 1.0 are repeated for clarity. The magnitude scale for the WISE observations is arbitrarily offset to provide the best fit to the model curve. The plot shows that the WISE observations of Leucus were acquired near the lightcurve minimum.

nonstandard photometric systems, are subject to inaccurate calibrations, and are therefore affected by large uncertainties. A further reason for the discrepancy is that the WISE observations happen to have occurred in the vicinity of the lightcurve minimum (see Figure 8), thereby underestimating the average thermal flux of Leucus. If we use our value $H_{V-LSL} = 10.979$ to correct their determination by using the method proposed by Harris & Harris (1997) and account for the apparent visible cross-section at the time of the WISE observations, we obtain a corrected geometric albedo $p_V = 0.048 \pm 0.014$ and a diameter $D = 39 \pm 1$ km. With these corrections applied, the WISE determinations are compatible with our own within the respective uncertainties.

The IRAS albedo and size determinations by Tedesco et al. (2004; 0.063±0.014 and 42.2 ± 4.0 km, respectively) were based on an inaccurate H value of 10.5. By using our H_{V-LSL} value we update their determinations to $p_V = 0.041 \pm 0.014$ and $D = 41.9 \pm 4.0$, which are also in agreement with our own determinations.

Buie et al. (2020) determined geometric albedo values for the four occultation events in 2018 and 2019 by estimating the object cross-sectional area from best-fit ellipses and by using the absolute photometry reported in this paper. They derived geometric albedo values ranging from 0.035 to 0.043 for the different occultation events with the scatter of the measurements probably reflecting the uncertainty in the different elliptical approximations of the occultation profiles.

5. Discussion

The combination of time-resolved, disk-integrated photometry and stellar occultations is a powerful technique that allows accurate characterization from the ground of otherwise unresolved targets. We have determined a convex shape model that is compatible with the available occultation footprints and, thanks to accurate absolute photometry, produces precise size and albedo estimates of Leucus. Our model also allows us to understand and correct previous incompatible radiometric albedo and size determinations.

The accuracy of our rotation model is such that the 1σ uncertainty on the rotation phase will be smaller than 2° at the time of the June 2028 Lucy encounter with Leucus. At the time of the flyby, the subsolar latitude will be about −9° and the south pole will be permanently illuminated—although at grazing incidence—whereas the north pole will be in its winter night. Unfortunately, due to the slow rotation of the body, Lucy will be able to observe at most 60% of the surface in the 40 hours during which the object will be resolved with more than 40 pixels. For this reason, an accurate ground-based shape model is very valuable to the mission. On the one hand it enables careful planning of the acquisition sequences, in order to guarantee optimum sampling. On the other hand, it complements the data from the mission to complete the uncharted hemisphere, similarly to what was done, e.g., in the case of the Rosetta flyby of Lutetia (Carry et al. 2010; Preusker et al. 2012). The latter is of crucial importance for the estimation of the volume of the object and hence of its bulk density. Our convex model already serves this purpose well and represents a good second-order approximation of the shape—the first order being an ellipsoid (Buie et al. 2020).

With an angular size of the longest axis of 15 mas at most, Leucus represents a challenging target to resolve for ground-based adaptive optics, the James Webb Space Telescope, or ESO's ALMA observations. Further improvement of the shape model in the near future can likely only come from dense stellar occultation data at further geometries and from more accurate absolute lightcurves. These data could be possibly used to produce a realistic nonconvex model provided the observation geometries are favorable. In this respect it is important to recall that not all concavities are directly resolvable from stellar occultations. A Star Wars Death-Star shape, for example, would always project a convex occultation silhouette, with its concavity only being hinted at by a flat side of the contour.

Our photometric modeling of Leucus confirms that the object is very dark and lacks a pronounced opposition effect. These properties put Leucus in the context of other Trojan asteroids, and of other primitive, Outer-Belt objects. Due to the limited phase angle range achievable from Earth, however, we caution from extrapolating the derived phase curve to predict the brightness of Leucus at the large phase angles occurring on Lucy approach (>90°), because it could be in error by a considerable factor. For this purpose it will be important to benefit from Lucy's vantage point during the cruise phase to extend the coverage of the phase curve to larger angles. Such measurements would also allow the use of more sophisticated photometric models and to uniquely retrieve their parameters. Further, they would allow a reliable determination of the phase integral, which, together with the geometric albedo, is critical to establish the thermal balance of the body.

Leucus exhibits an exceptionally slow rotation, the cause of which is currently not known. As of today, only about 0.8% of the about 32,600 asteroids in the Asteroid Lightcurve Data Base (LCDB; Warner et al. 2009) for which rotation period estimates are available, have a slower spin than Leucus. Objects with such slow rotation cannot be explained as just belonging to the tail of a single population of rotators (Harris 2002), and some mechanism must have been in place that slowed down their rotation. Radiation recoil forces as the YORP effect (Rubincam 2000) cannot explain the slow rotation of Leucus because of its large size and heliocentric distance. More realistic possibilities are (1) rotation angular momentum loss due to the evolution and eventual separation of a binary system with an elongated primary (Harris 2002) and (2)

spin-down due to reaction forces resulting from sublimation of volatiles.

Pravec et al. (2014) revised the damping timescales for excited rotation as a function of asteroid size and rotation period. By assuming a bulk density for Leucus of 1×10^3 kg m^{-3}, their estimate would translate into a relaxation time for Leucus in the range 2.3–3.0 Gyr. If excited rotation was ever present for Leucus it could be still in place as of today. Given the good fit of the lightcurves to our simple-rotation model, however, we conclude that if an excited rotation is present, its precession amplitude must be small. Due to the short duration of the flyby, it is unlikely that any degree of precession can be detected by Lucy from resolved imagery. Instead, unresolved photometric sequences acquired by Lucy during the last few months of approach could be used to search for multiple periodicities in the lightcurves. The detection of a nonprincipal rotation state would place additional constraints on the dynamics and the internal structure of Leucus.

Research at the DLR was funded by the *DLR Programmatik Raumfahrtforschung und -technologie* through the grant 2474029 *Lucy*. Part of this work was supported by the Lucy Mission which is funded through the NASA Discovery program on contract number NNM16AA08C. This work was partly based on observations collected at the Centro Astronómico Hispano-Alemán (CAHA) at Calar Alto.

Appendix
Photometric Quantities

For the convex shape inversion we use a photometric function defined as the product of a Lommel-Seeliger–Lambert disk function and a three-parameter linear-exponential surface phase function (Kaasalainen et al. 2001; Schröder et al. 2013). The corresponding *radiance factor* (I/F) can be written as:

$$I/F = A_{\rm LSL}\ \mu_0 \left(\frac{1}{\mu + \mu_0} + c \right) f(\alpha), \tag{A1}$$

where $A_{\rm LSL}$ is the Lommel-Seeliger–Lambert albedo, μ_0 and μ are the incidence and emission angles, respectively, and c is the weight for the Lambert contribution. The term c can be either constant, or a function of the phase angle α. In the latter case the Lommel-Seeliger–Lambert disk function is equivalent to the Lunar-Lambert disk function in the formulation of McEwen (1996). The term $f(\alpha)$ is the surface phase function (expressed in intensity), which, following Kaasalainen et al. (2001) we choose to be of the form:

$$f(\alpha) = A_0\ e^{-\alpha/D} + k\alpha + 1, \tag{A2}$$

where A_0 and D are parameters that determine the amplitude and angular width of the exponential term, respectively, and k is the slope of the linear component. The phase angle α is expressed in radians. With this formalism the geometric albedo for a sphere is:

$$p_V = A_{\rm LSL} \left(\frac{1}{2} + \frac{2}{3} c_0 \right) (A_0 + 1), \tag{A3}$$

where c_0 is the value of the Lambert weight at zero phase angle.

The disk-integrated phase function for a sphere, expressed in intensity and normalized to unity at zero phase is (Li et al. 2015, 2020):

$$\Phi_{\rm LSL}(\alpha) = \frac{[4c/(3\pi)\,(\sin(\alpha) + (\pi - \alpha)\cos(\alpha)) + (1 + \sin(\alpha/2)\ln(\tan(\alpha/4))\tan(\alpha/2))]}{(4c_0/3 + 1)} \frac{f(\alpha)}{(A_0 + 1)}. \tag{A4}$$

ORCID iDs

Stefano Mottola https://orcid.org/0000-0002-0457-3872
Marc W. Buie https://orcid.org/0000-0003-0854-745X

References

Archinal, B. A., Acton, C. H., A'Hearn, M. F., et al. 2018, CeMDA, 130, 22
Archinal, B. A., Acton, C. H., Conrad, A., et al. 2019, CeMDA, 131, 61
Bellm, E. C., Kulkarni, S. R., Graham, M. J., et al. 2019, PASP, 131, 018002
Bertin, E., & Arnouts, S. 1996, A&AS, 117, 393
Bowell, E., Hapke, B., Domingue, D., et al. 1989, in Asteroids II, ed. R. P. Binzel, T. Gehrels, & M. S. Matthews (Tucson, AZ: Univ. Arizona Press), 524
Buie, M. W., Keeney, B. A., Strauss, R. H., et al. 2020, PSJ, submitted
Buie, M. W., Zangari, A. M., Marchi, S., Levison, H. F., & Mottola, S. 2018, AJ, 155, 245
Carry, B., Kaasalainen, M., Leyrat, C., et al. 2010, A&A, 523, A94
Dobrovolskis, A. R. 1996, Icar, 124, 698
Durech, J., Kaasalainen, M., Herald, D., et al. 2011, Icar, 214, 652
Durech, J., Sidorin, V., & Kaasalainen, M. 2010, A&A, 513, A46
Evans, D. W., Riello, M., De Angeli, F., et al. 2018, A&A, 616, A4
Flewelling, H. A., Magnier, E. A., Chambers, K. C., et al. 2016, arXiv:1612.05243
French, L. M., Stephens, R. D., Coley, D. R., et al. 2013, MPBu, 40, 198
Gaia Collaboration, Spoto, F., Tanga, P., et al. 2018, A&A, 616, A13
Grav, T., Mainzer, A. K., Bauer, J. M., Masiero, J. R., & Nugent, C. R. 2012, ApJ, 759, 49
Green, R. M. 1985, Spherical Astronomy (Cambridge: Cambridge Univ. Press)
Hapke, B. 2012, Icar, 221, 1079
Harris, A. W. 2002, Icar, 156, 184
Harris, A. W., & Harris, A. W. 1997, Icar, 126, 450
Harris, A. W., Young, J. W., Bowell, E., et al. 1989, Icar, 77, 171
Harris, A. W., Young, J. W., Scaltriti, F., & Zappala, V. 1984, Icar, 57, 251
Henden, A. A., Levine, S. E., Terrell, D., Smith, T. C., & Welch, D. 2012, JAVSO, 40, 430
Kaasalainen, M., & Lamberg, L. 2006, InvPr, 22, 749
Kaasalainen, M., Lu, X., & Vänttinen, A. V. 2012, A&A, 539, A96
Kaasalainen, M., Mottola, S., & Fulchignoni, M. 2002, in Asteroids III, ed. W. F. Bottke, Jr. (Tucson, AZ: Univ. Arizona Press), 139
Kaasalainen, M., & Torppa, J. 2001, Icar, 153, 24
Kaasalainen, M., Torppa, J., & Muinonen, K. 2001, Icar, 153, 37
Kaasalainen, M., & Viikinkoski, M. 2012, A&A, 543, A97
Kaasalainen, S., Kaasalainen, M., & Piironen, J. 2005, A&A, 440, 1177
Kubica, J., Denneau, L., Grav, T., et al. 2007, Icar, 189, 151
Lamberg, L. 1993, PhD thesis, Univ. Helsinki
Lebedev, V. I., & Laikov, D. N. 1999, Doklady Mathematics, 59, 477
Levison, H. F. & Lucy Science Team 2016, LPSC, 47, 2061
Li, J. Y., Helfenstein, P., Buratti, B., Takir, D., & Clark, B. E. 2015, in Asteroids IV, ed. P. Michel, F. E. DeMeo, & W. F. Bottke (Tucson, AZ: Univ. Arizona Press), 129
Li, J.-Y., Helfenstein, P., Buratti, B. J., Takir, D., & Clark, B. E. 2020, Icar, 337, 113354
McEwen, A. S. 1996, LPCS, 27, 841
Minkowski, H. 1897, NWGot, 1897, 198, http://eudml.org/doc/58391
Morbidelli, A., Levison, H. F., Tsiganis, K., & Gomes, R. 2005, Natur, 435, 462
Mottola, S., De Angelis, G., Di Martino, M., et al. 1995, Icar, 117, 62

Muinonen, K., Belskaya, I. N., Cellino, A., et al. 2010, Icar, 209, 542
Nesvorný, D., Vokrouhlický, D., & Morbidelli, A. 2013, ApJ, 768, 45
Oszkiewicz, D. A., Bowell, E., Wasserman, L. H., et al. 2012, Icar, 219, 283
Penttilä, A., Shevchenko, V. G., Wilkman, O., & Muinonen, K. 2016, P&SS, 123, 117
Pravec, P., Scheirich, P., Ďurech, J. J., et al. 2014, Icar, 233, 48
Press, W. H., Teukolsky, S. A., Vetterling, W. T., & Flannery, B. P. 1992, Numerical Recipes in C. The Art of Scientific Computing (2nd ed.; Cambridge: Cambridge Univ. Press)
Preusker, F., Scholten, F., Knollenberg, J., et al. 2012, P&SS, 66, 54
Roig, F., Ribeiro, A. O., & Gil-Hutton, R. 2008, A&A, 483, 911
Rubincam, D. P. 2000, Icar, 148, 2
Schröder, S. E., Mottola, S., Keller, H. U., Raymond, C. A., & Russell, C. T. 2013, P&SS, 85, 198
Shevchenko, V. G., Belskaya, I. N., Muinonen, K., et al. 2016, P&SS, 123, 101
Shevchenko, V. G., Belskaya, I. N., Slyusarev, I. G., et al. 2012, Icar, 217, 202
Shoemaker, E. M., Shoemaker, C. S., & Wolfe, R. F. 1989, in Asteroids II, ed. R. P. Binzel, T. Gehrels, & M. S. Matthews (Tucson, AZ: Univ. Arizona Press), 487
Tabur, V. 2007, PASA, 24, 189
Tedesco, E. F., Noah, P. V., Noah, M., & Price, S. D. 2004, IRAS-A-FPA-3-RDR-IMPS-V6.0, NASA Planetary Data System, https://sbn.psi.edu/pds/resource/imps.html
Tonry, J. L., Denneau, L., Heinze, A. N., et al. 2018, PASP, 130, 064505
Torppa, J., Hentunen, V. P., Pääkkönen, P., Kehusmaa, P., & Muinonen, K. 2008, Icar, 198, 91
Viikinkoski, M., Kaasalainen, M., & Durech, J. 2015, A&A, 576, A8
Warner, B. D., Harris, A. W., & Pravec, P. 2009, Icar, 202, 134
Yoder, C. F. 1979, Icar, 40, 341